Simulation of the melt season using a resolved sea ice model with snow cover and melt ponds

Citation	Skyllingstad, E. D., Shell, K. M., Collins, L., & Polashenski, C. (2015). Simulation of the melt season using a resolved sea ice model with snow cover and melt ponds. Journal of Geophysical Research: Oceans, 120(7), 5194-5215. doi:10.1002/2014JC010569
DOI	10.1002/2014JC010569
Publisher	John Wiley & Sons, Inc.
Version	Version of Record
Terms of Use	http://cdss.library.oregonstate.edu/sa-termsofuse

AGU PUBLICATIONS

JGR

Journal of Geophysical Research: Oceans

RESEARCH ARTICLE

10.1002/2014JC010569

Key Points:
- Melt ponds are dependent on snow cover depth at the start of the melt season
- Ponds are sensitive to snow depth, ice thickness, and ice variations
- Ice layers determine initial pond flooding and timing of pond drainage

Supporting Information:
- Supporting Information S1
- Supporting Information S2

Correspondence to:
E. D. Skyllingstad,
skylling@coas.oregonstate.edu

Citation:
Skyllingstad, E. D., K. M. Shell, L. Collins, and C. Polashenski (2015), Simulation of the melt season using a resolved sea ice model with snow cover and melt ponds, *J. Geophys. Res. Oceans*, *120*, 5194–5215, doi:10.1002/2014JC010569.

Received 6 NOV 2014
Accepted 11 JUN 2015
Accepted article online 16 JUN 2015
Published online 27 JUL 2015

Simulation of the melt season using a resolved sea ice model with snow cover and melt ponds

Eric D. Skyllingstad[1], Karen M. Shell[1], Lee Collins[1], and Chris Polashenski[2]

[1]College of Earth, Ocean, and Atmospheric Sciences, Oregon State University, Corvallis, Oregon, USA, [2]Cold Regions Research and Engineering Laboratory, U. S. Army Engineer Research and Development Center, Hanover, New Hampshire, USA

Abstract A three-dimensional sea ice model is presented with resolved snow thickness variations and melt ponds. The model calculates heating from solar radiative transfer and simulates the formation and movement of brine/melt water through the ice system. Initialization for the model is based on observations of snow topography made during the summer melt seasons of 2009, 2010, and 2012 from a location off the coast of Barrow, AK. Experiments are conducted to examine the importance of snow properties and snow and ice thickness by comparing observed and modeled pond fraction and albedo. One key process simulated by the model is the formation of frozen layers in the ice as relatively warm fresh water grid cells freeze when cooled by adjacent, cold brine-filled grid cells. These layers prevent vertical drainage and lead to flooding of melt water commonly observed at the beginning of the melt season. Flooding persists until enough heat is absorbed to melt through the frozen layer. The resulting long-term melt pond coverage is sensitive to both the spatial variability of snow cover and the minimum snow depth. For thin snow cover, initial melting results in earlier, reduced flooding with a small change in pond fraction after drainage of the melt water. Deeper snow tends to generate a delayed, larger peak pond fraction before drainage.

1. Introduction

Accurate representation of sea ice processes in earth system climate models is critical for simulating potential changes in the climate system. Recent decreases in ice coverage and ice thickness distributions [*Stroeve et al.*, 2007; *Perovich and Richter-Menge*, 2009] have been linked to both large-scale changes in ice transport and increased summer melting from the ice-albedo feedback. A key element in the local ice-albedo feedback is the presence of melt ponds on the ice surface [*Schröder et al.*, 2014]. Melt ponds typically have a much lower albedo than surrounding sea ice and can transmit solar radiation more directly into the upper ocean [*Inoue et al.*, 2008]. As ponds form, they absorb more solar radiation, which is then available to increase the ice-melting rate in a nonlinear feedback process. Eventually, ponds can melt completely through the ice, decreasing the ice integrity so that wind forcing can generate ice breakup.

Melt ponds depend critically on the underlying ice structure, with pond formation and evolution strongly tied to the ice and snow cover conditions that exist at the beginning of the summer melt season. On first-year ice, ponds form early in summer as snow melts and floods the ice surface. After several days, flaws in the ice provide pathways for ponds to drain to the ocean, with remaining ponds limited to regions of the ice surface that are below sea level [*Polashenski et al.*, 2012]. Initial flooding of the ice surface produces a pond fractional coverage ranging from 40 to 70%, depending on the topography of the snow surface and timing of the pond drainage through ice flaws [*Polashenski et al.*, 2012]. After the ice drains, sea-level ponds cover a decreased area ranging from 10 to 20% and then grow in size and depth at a more gradual rate until either they melt through the ice or the ice breaks up from structural weakness and wind forcing.

Eicken et al. [2002] describe this sequence of events in four stages with stage 1 representing the flooding of the ice, stage 2 the drainage, stage 3 ponds at sea level, and finally stage 4 ice breakup or ponds refreezing. Examples of this behavior from three melt seasons are shown in Figure 1 along with the three corresponding stages of pond evolution for 2009. In 2009 (black line), pond area fraction peaks early in June followed by a rapid decline and then a much more gradual increase over the remainder of the month. In 2010 (red line) and 2012 (blue line), pond fraction increases later than in the 2009 case and decreases gradually from the peak flooding in mid June, suggesting that stage 2 persists for much of the measured time period for

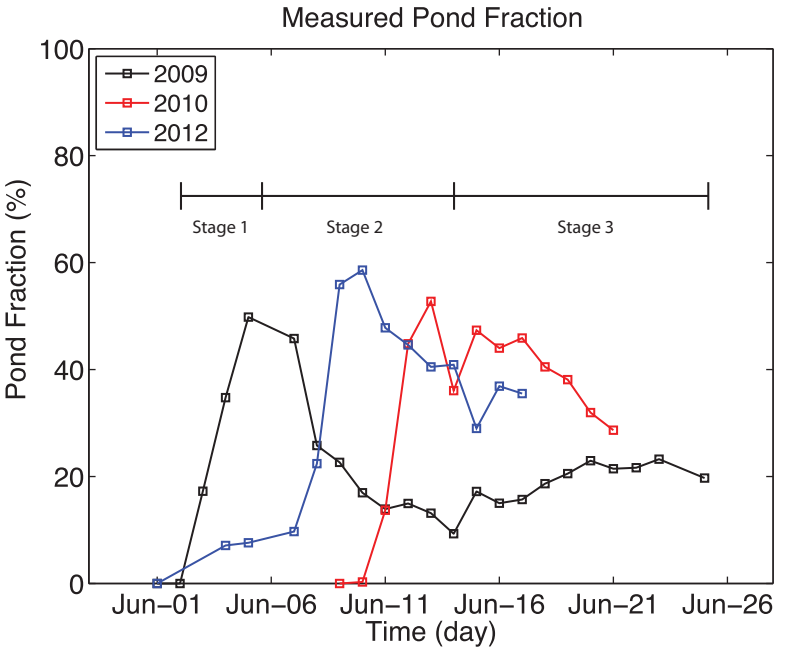

Figure 1. Measured pond fraction (percent of points covered with a pond) along a 200 m long survey line near the Barrow, AK ice mass balance site during three melt seasons. Also shown schematically are the three stages of melt pond evolution for year 2009.

these two years. Both short and long stage 2 periods are commonly observed for sea ice off the coast of Barrow [*Polashenski et al*., 2012] and are not well understood. For example, we do not know what factors lead to earlier flooding and why some cases drain more rapidly than others.

First-year ice is typically less deformed in comparison with older ice, and observations indicate that ponds initially form in regions with thin snow cover between snow drifts or snow dunes on top of the relatively flat first-year ice. Snow dunes depend on the amount of snow and wind produced by winter storms, indicating that winter weather conditions may be important in determining the location and size of ponds on level first-year ice [*Petrich et al*., 2012]. The low topographic variation can lead to a large extent of surface flooding. In contrast, ponds on multiyear ice typically form in preexisting ice depressions created by either old frozen ponds or through ice deformation from ice motion. Surface ice flooding is less prevalent on multiyear ice, and ponds tend to grow steadily over a more limited area during the summer melt season [*Perovich et al*., 2003]. Surface summer albedo values for multiyear ice are consequently higher in comparison with first-year ice because of smaller pond fractional coverage.

The importance of melt ponds has been highlighted in recent climate modeling experiments. Including more realistic melt pond processes improves modeled sea ice interannual variability [*Flocco et al*., 2012; *Hunke et al*., 2013a]. Sea ice melting is difficult to parameterize because of the importance of meter-scale ice features such as melt ponds and leads, as well as submeter-scale structures including ice flaws and brine channels. Current pond parameterizations, for example as used in the CICE model [*Hunke et al*., 2013a], calculate pond coverage based on the volume of melted surface snow and ice along with variations in ice thickness categories. This approach simulates summer pond evolution for a basic ice surface, taking into account possible dependences of pond coverage on snow depth and the fraction of undeformed ice in a grid cell. Details, such as the impact of snow dunes and ice surface flooding, are not specifically included in these parameterizations.

Our goal is to better understand the processes that determine pond coverage and evolution during the summer melt season by applying a high-resolution sea ice and pond model. The modeling approach follows similar ice-pond models presented in *Scott and Feltham* [2010], *Skyllingstad et al.* [2009], and *Lüthje et al*. [2006], but with greater emphasis placed on the role of surface snow cover in controlling the pond evolution. We use recently measured surface snow topography and pond coverage statistics collected at the Barrow Alaska observation site [*Polashenski et al*., 2012] to initialize the model and to validate the

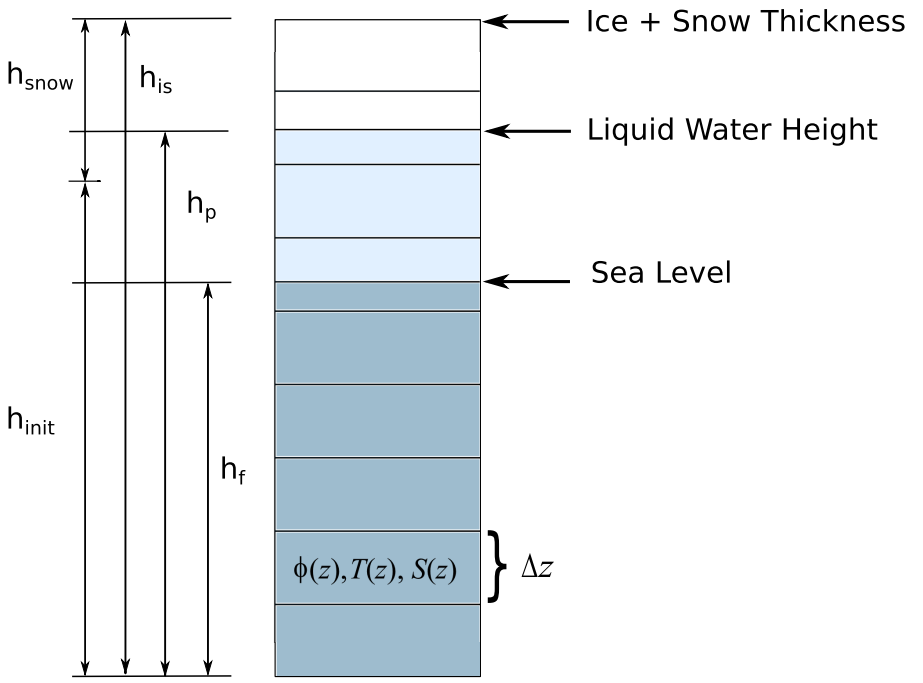

Figure 2. Schematic diagram of sea ice grid structure and key bulk parameters for a column before pond formation. Dark blue indicates ice filled with brine below sea level. Light blue levels contain sea ice or snow with the spaces filled with melted fresh water. The white levels correspond to snow (since they are above the initial sea ice thickness) with spaces filled with air.

model-predicted pond and ice characteristics. *Polashenski et al*. [2012] analyze sea ice evolution over an area of roughly 100 m × 200 m, mapping the ice surface morphology using a combination of LiDAR altimetry and aerial photos. These data provide a map of the initial snow cover height variations, along with the evolution of the surface topography and ponding from the beginning of the melt season until the ice was too unstable for continued field operations. Topography data were collected at the Barrow site for the 2009, 2010, and 2012 melt seasons, with the 2009 season providing the most complete observation set. Here we use these data to initialize our simulations and provide a means for adjusting model parameters. Our goal is to determine which features and processes are critical in the formation and evolution of ponds.

We begin with a description of the resolved sea ice model (hereafter RSIM) in section 2. Section 3 describes the model initialization and forcing. In section 4, we perform a series of sensitivity experiments using measurements taken near the Barrow, AK field site, to calibrate the model and analyze the roles of initial snow depth, sea ice thickness, and atmospheric forcing on pond formation and ice melting rates. Section 5 compares the calibrated model to field observations. The paper concludes with a summary of our results and discussion of the implications of this work for sea ice parameterization in climate system models.

2. Model Description

Our approach extends previous modeling work of *Skyllingstad et al*. [2009] and *Skyllingstad and Paulson* [2007]. These two studies examine the heat budget of melt ponds and develop a horizontally two-dimensional model of pond growth on level ice. Here we add a melt-water budget that allows for ponds on nonporous sea ice. We also include the vertical structure of the ice porosity, salinity, and temperature. And incorporate a more realistic calculation of shortwave radiative transfer through ice, snow, and ponds using the delta-Eddington method taken from the CICE model [*Hunke et al*., 2013b; *Briegleb and Light*, 2007]. These improved representations, in addition to allowing the model to simulate many more scenarios, will enable a better comparison of model behavior between our resolved sea ice model (RSIM) and CICE in later work.

The model consists of a hybrid two- and three-dimensional system with two-dimensional properties, such as ice thickness, ($h_{is}(x,y)$), and a three-dimensional grid with each grid column containing a mixture of sea ice, snow, water, and air as shown schematically in Figure 2. The volume fraction for each component can

be deduced from the ice (including both sea ice and snow) volume fraction ($\phi(x,y,z)$) and the location of the cell relative to both the water table and the initial sea ice thickness (throughout the paper we follow *Feltham et al*. [2006] and refer to the ice volume fraction ϕ and void fraction $1-\phi$ in describing the porosity of the ice/snow). Within a grid cell, a single temperature ($T(x,y,z)$) represents both solid and liquid water, and the bulk salinity ($S_{bulk}(x,y,z)$) the total amount of salt. For each column, $h_{is}(x,y)$ is the distance from the bottom of the ice to the top of the snow (or sea ice, if there is no snow). The sea level h_f is the distance from the bottom of the ice to sea level, and space within the ice (void fraction, $1-\phi$) is always filled with brine below h_f. In the freeboard above h_f, spaces in the ice are filled with fresh melt water up to the water table height h_p. Thermodynamically, the grid point is considered a pond when $h_p > h_{is} + 0.02$ m, with the pond modeled as an independent layer having uniform water temperature (for radiative purposes, ponds are defined differently as described below). We chose the 0.02 m threshold to ensure a pond depth of at least two vertical grid levels in the model (see supporting information for more details on the grid structure). Sea level is determined in the model after each time step by summing the total ice, liquid water, and snow mass and calculating the displacement. The basic model equations for predicting snow, ice, and pond temperature, along with surface and bottom heating and cooling terms, are presented in the supporting information section.

Shortwave radiative transfer through the ice system is calculated using the delta-Eddington method taken from the CICE model [*Hunke et al*., 2013b]. One of three surface types, snow, pond, or ice, is set for each grid point depending on the water table height and the snow/ice height at any given time. These surface types are used by the radiative transfer scheme to determine shortwave radiative absorption and the grid point albedo. CICE uses a prescribed number of levels for ice, with layer thicknesses varying depending on the ice thickness. In contrast, we apply a variable number of ice levels of the same thickness, depending on the vertical grid resolution and h_{is}. As in CICE, snow and ponds are treated as one-layer systems depending on the depth of the snow cover and the water table depth (h_p) relative to the ice thickness (h_{is}). Snow depth is prescribed at the beginning of each simulation and decreases through melting. We set the surface type as snow until the snow depth is zero, and snow depth is set to a minimum of 0.02 m in the radiation scheme. We also designate a snow or ice surface as a pond of depth 0.01 m in the radiation scheme when the local water level, as indicated by h_p, exceeds the surface height h_{is} by less than 0.02 m. Our assumption here is that the albedo decreases when the surface is saturated with water, but subgrid-scale variations in the surface ice/snow cover produce a surface that is not entirely water covered. Consequently, we do not apply the pond thermodynamic model in these shallow pond cases (resolved thermodynamic ponds require a depth of 0.02 m), but assume the top grid point is completely water-filled ice or snow for radiative transfer calculations.

Variations in h_{is} are controlled by surface and bottom melting of individual grid cells. Ice in the model domain is assumed to be a rigid floe without dynamic effects such as keel growth or leads. Surface (Δh_{top}) and bottom (Δh_{bot}) melting result in a discrete change in the bulk thickness value (Δh_{is}) per time step ($\Delta t = 600$ s) for each 2-D grid point:

$$\Delta h_{is} = \Delta h_{top} + \Delta h_{bot} \tag{1}$$

where $\Delta h_{bot} = -w_{bot}\Delta t$, w_{bot} (m s^{-1}) is the (constant) bottom melting rate, Δt is the model time step, and Δh_{top} is derived from the sum of surface solar, long wave, sensible, and latent heating along with conduction and transport of heat into the ice/snow, defined in the supporting information section.

The water table, h_p, is calculated by tracking the quantity of melt water produced at each horizontal grid point location. Melt water is produced in each grid cell by reductions in the snow and ice volume fraction (i.e., internal melting) and at the surface by decreases in sea ice or snow thickness (i.e., surface melting). Bottom melting results in a direct reduction in h_{is} and h_p, requiring a recalculation of h_f based on the total grid point ice mass displacement. We calculate the total melt water volume m_w using,

$$\frac{dm_w}{dt} = -\sum_{x,y}\left\{\sum_{z=h_f}^{h_{is}(x,y)}\frac{\rho_w}{\rho_i}\frac{d\phi(x,y,z)}{dt} + \frac{\partial h_{is}}{\partial t}\frac{\rho_w}{\rho_i}\frac{\phi_{top}}{\Delta z} - \frac{\rho_w}{\rho_i}\frac{w_{darc}}{\Delta z}\right\} \tag{2}$$

where ϕ_{top} is the sea ice or snow volume fraction of the top layer and w_{darc} is a vertical Darcy velocity ($w_{darc} \leq 0$ in the current implementation). Changes in the ice fraction ϕ below h_f are not considered in the

melt water budget because brine channels in these grid cells are assumed to be always full of water. Above h_f, void regions in ice and snow may be filled with air rather than water or brine. Melt water is assumed to immediately settle to the lowest level above sea level, allowing h_p to be calculated by summing the ice void fractions upward from sea level h_f until the vertically integrated void fraction (the ice volume fraction subtracted from one) equals the total melt water fraction,

$$\sum_{x,y} \sum_{z=h_f}^{h_p(x,y)} (1-\phi(x,y,z)) = m_w \tag{3}$$

where by definition, h_p has a minimum of h_f. This integration has the net effect of moving melt water instantaneously across the horizontal ice/snow surface each time step. We justify this assumption by noting that observations of the water table during pond events indicate very little height difference across the ice surface.

Vertical transport of melt water above sea level is modeled using standard Darcy flow ground water methods that depend on the ice permeability and local pressure head, following *Scott and Feltham* [2010]. A key aspect of our model is that we use observations of melt pond behavior to calibrate the ice permeability coefficient to accurately simulate the melting process, flooding, and pond drainage. The Darcy velocity is calculated using

$$w_{darc} = -\pi_v \frac{g\rho_w}{\mu} \frac{(h_p - h_f)}{h_{is}} \text{ for } h_p > h_f, \quad \text{otherwise } w_{darc} = 0.0, \tag{4}$$

where $g = 9.81$ m s^{-2} is the gravitational acceleration, $\rho_w = 1000$ kg m^{-3} is the water density, $\mu = 10^{-3}$ kg m^{-1} s^{-1} is the dynamic viscosity of water, and π_v is the vertical permeability. We set ice permeability values based on the observed behavior of melt ponds reported in *Polashenski et al*. [2012] combined with the semiempirical formula for permeability introduced by *Golden et al*. [2007],

$$\pi_v = \Pi_v (1-\phi)^3 \text{m}^2. \tag{5}$$

A constant vertical permeability coefficient of $\Pi_v = 1 \times 10^{-10}$ is determined through an ensemble of simulations presented below in section 4. This value is notably lower than the *Golden et al*. [2007] estimate for cold season, brine-filled ice where $\Pi = 3 \times 10^{-8}$. We also note that this parameterization does not directly take into account retention of melt water by capillary action in snow or ice, although these effects may be partially explained through our calibration process.

Eicken et al. [2004] suggest that the vertical permeability is a key parameter that sets the timing and extent of pond coverage. They, along with *Polashenski et al*. [2012] and *Landy et al*. [2014], hypothesize that when surface melt of snow begins, fresh water drains onto the ice and forms impermeable frozen layers. Frozen layers also form when fresh water drains into the upper ice and freezes in the vacated brine channels. Both processes effectively decrease the ice permeability by reducing the void fraction to near zero. As solar insolation increases, further internal warming of the ice from penetrative radiation eventually leads to melting of these channels so that fresh water trapped on the surface can drain and flush the remaining brine from the ice pores. At this time, snow melt water is typically above sea level. The water exerts a hydrostatic pressure head in the ice pores that effectively forces brine from the ice into the upper ocean until the melt water level equals sea level.

A key goal of our research was to construct an ice/snow model that could accurately predict the multistage pond behavior reported in *Eicken et al*. [2004], *Polashenski et al*. [2012] and *Landy et al*. [2014]. One important element of this model is the refreezing of fresh water in grid boxes just above sea level where it comes in contact with brine-filled ice that has a freezing point below zero. This refreezing of melt water in the upper portion of the ice above sea level is a critical process that controls the initial pond formation and timing of the pond drainage. When this ice eventually melts, our results suggest that a reduced permeability coefficient value, relative to *Golden et al*. [2007], is necessary to prevent rapid pond drainage. Through calibration of the permeability coefficient value, our model produces stable ponding behavior very similar to the observations when tuned with the correct snow and ice depth at the initial time step. Field observations from *Polashenski et al*. [2012] and *Landy et al*. [2014] clearly show that pond drainage differs greatly from drainage corresponding to standard sea ice brine permeability [*Golden et al*. 2007], and we find that the smaller values of Π_v, in comparison with the Golden formula, yield pond drainage more in line with their field studies.

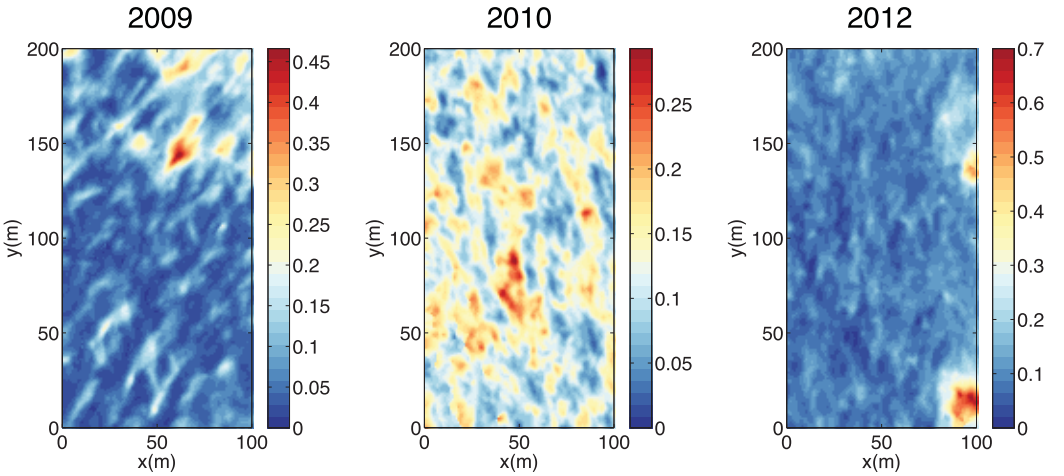

Figure 3. LiDAR-estimated initial snow surface elevation (m) for observation years 2009, 2010, and 2012. Ranges indicate the snow surface variations, but do not provide a snow thickness. Note difference in scales.

3. Initial Conditions and Forcing

Model resolution for experiments presented here is set to 1.0 m in the horizontal direction and 0.01 m in the vertical direction over a domain size of 100 m × 200 m, with cyclical horizontal boundary conditions. Initial ice thickness and snow depths are estimated from field observations collected off of Pt. Barrow, Alaska

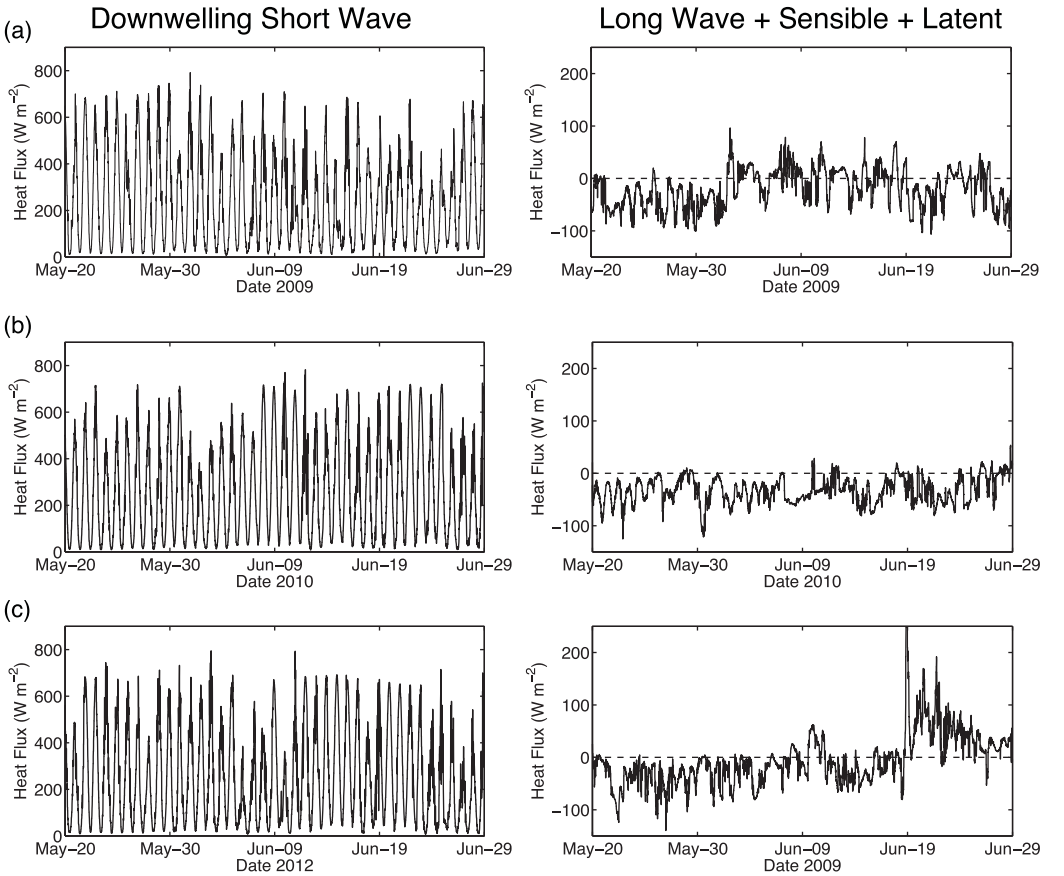

Figure 4. Surface fluxes from the Point Barrow Department of Energy Atmospheric Radiation Measurement (DOE-ARM) site for (a) 2009, (b) 2010, and (c) 2012. Scales differ between variables; positive values indicate surface warming, negative values cooling. Upward infrared, sensible, and latent heat fluxes are averaged over the model domain.

Table 1. Model Parameters Held Constant in Each Simulation[a]

Parameter	Value
Bottom melt rate	0.01 m d^{-1}
ρ_{snow}	460 kg m^{-3}
Snow grain size	500 μm

[a]Snow density is based on observations of old snow reported in *Jonas et al.* [2009].

Table 2. Internal Parameter Values Used in Calibration[a]

Parameter	Range
Π_v (m^2)	5×10^{-11}, $\mathbf{1 \times 10^{-10}}$, 1.5×10^{-10}, 3×10^{-10}, 1×10^{-9}

[a]Optimal value is in bold.

(71.366 N, 156.542 W) during the melt seasons of 2009, 2010, and 2012. The initial vertical sea ice thickness is horizontally uniform, with values between 1.2 and 1.6 m, inclusive, depending on the particular simulation. This range is derived from measurements from the University of Alaska-Fairbanks ice mass balance site [*Eicken et al.*, 2012] near the LiDAR (or field) observation site at the simulation start date. Because measurements of ice thickness are limited to only a few locations, we consider an ensemble of initial ice thicknesses in testing the ice model.

Initial snow surface variations are based on LiDAR observations described in *Polashenski et al.* [2012] and represent 3 years with different melt pond behavior as shown by Figure 2. LiDAR data typically have horizontal resolution as fine as 0.1 m, although simulations here are conducted using a smoothed data set with resolution of 1.0 m, rotated and interpolated to a uniform grid using a *Barnes* objective analysis scheme [*Barnes*, 1964]. The LiDAR data provide relative heights for the snow depths, but it does not measure the snow thickness relative to the underlying ice. LiDAR estimated initial snow surface elevation plots, relative to a minimum of zero, are shown in Figure 3 for each of the three cases. For each year, we specify the total depth of the snow by adding a horizontally constant "minimum snow depth" or h_{msd}, to the elevation data presented in Figure 3. As with the initial ice thickness, we examine an ensemble of h_{msd} that are within the range of measurements taken along a 200 m transect adjacent to the LiDAR scan area for each case. The initial snow depth (initial h_{snow}) is the sum of the relative thickness from LiDAR data shown in Figure 3 plus the optimal h_{msd} for each ensemble simulation. The sum of the initial sea ice thickness, h_{init}, and the initial snow depth, h_{snow}, is the initial sea ice/snow height h_{is} (Figure 1). Sensitivity experiments presented later in the paper indicate that both h_{msd} and h_{init} have a significant impact on the formation and evolution of melt ponds in the model. The values used in baseline simulations presented below were selected based on both observations and sensitivity tests to yield the most accurate pond fraction time series.

Simulations are conducted for a 40 day period beginning on 20 May, when observed ice has a brine salinity value near that of the underlying sea water. Ice internal temperatures are set to the brine freezing point temperature, T_{fr}, for ice below the water table and -4.0°C for ice and snow that is not brine-filled. Bulk ice salinity is set to 4 psu below 0.1 m ice depth with a linear decrease from 4 to 0 psu at the ice/snow interface. These initial profiles are similar to field measurements reported in *Polashenski et al.* [2012] during the middle of May in 2009. Initial ice volume fraction, ϕ, in the model is set to 0.5 for snow and 0.88 for ice. Snow density with this volume fraction is 460 kg m^{-3}, which is appropriate for old, melting snow [*Jonas et al.*, 2009].

Surface downwelling shortwave and longwave radiative fluxes are set using observed data from the Department of Energy-Atmospheric Radiation Measurement (ARM) program North Slope site located at Pt. Barrow, Alaska. Measurements of surface air temperature, relative humidity, and wind speed from the ARM site are used to compute sensible and latent heat fluxes and upwelling longwave flux. Details of these calculations are included in the supporting information. Plots of the combined net total longwave, sensible, and latent heat fluxes are shown in Figure 4 for each year in our study, with positive values indicating a net warming of the ice. Figure 4 also shows downwelling shortwave radiative flux, with positive values again indicating a warming of the surface. For most of the melt season, the sum of the longwave, sensible, and latent heating fluxes represents cooling, with only a few periods of significant warming. Thus, most of the heating for melting of sea ice comes from the downwelling shortwave radiation. This is in agreement with surface flux observations measured using eddy covariance methods during the SHEBA field experiment [*Persson et al.*, 2002], suggesting that our bulk estimates are reasonable.

Table 3. Initial Ice Thickness and Minimum Snow Depth Ranges Considered for Each Simulated Year

Ice Thickness (m)	Minimum Snow Depth (m)
1.2, 1.3, 1.4, 1.5, 1.6	0.09, 0.1, 0.12, 0.13, 0.14, 0.15

4. Model Calibration and Initial Conditions

The 3 years described above are used to calibrate the model over a range of snow and sea ice characteristics.

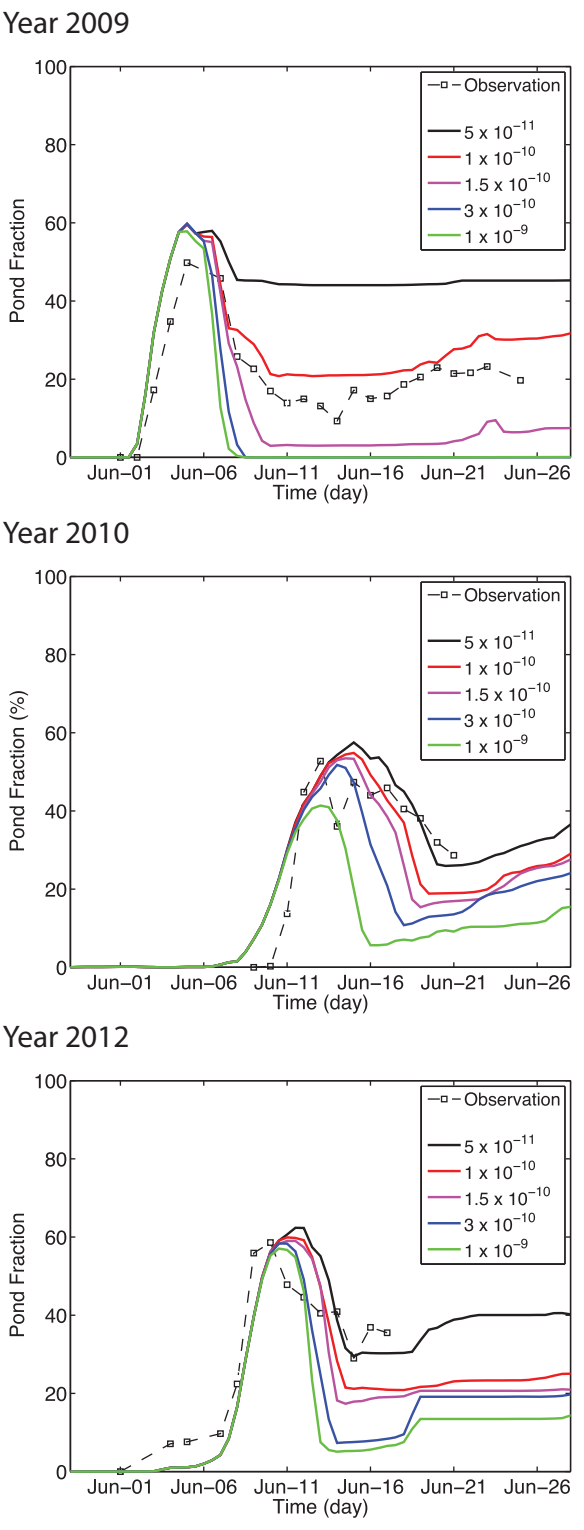

Figure 5. Simulated pond fractions (%) for optimal initial conditions and different permeability coefficient (m^2) values for (a) 2009, (b) 2010, and (c) 2012. Also plotted are the measured pond fractions (dashed) from the single lines of field measurements from Barrow, AK.

Two types of parameters can be varied in our model. "Internal" model parameters, such as the vertical permeability coefficient, quantify physical processes, which should be consistent for all simulations. "Initial conditions" represent the initial snow and sea ice state of the model for a particular time. Thus, internal parameters should be the same for all simulations (following calibration), while the initial conditions are different for each year. Our goal in these experiments is to determine a standard set of "internal" model parameters that will yield stable and accurate ponding behavior for all years considered and to explore the sensitivity of the ponding behavior to differences in initial conditions.

Because we have only rough estimates of these parameters for each simulation year, ranges of values are used to optimize the model accuracy over all three years. Numerous ensemble experiments (not presented here) were conducted to narrow the scope of key initial condition variables to the initial minimum snow depth and the initial ice thickness. Other initial variables, for example, the initial snow and sea ice temperature, did not significantly change the pond behavior over a range of realistic values. Similarly, numerous simulations (not presented here) identified the vertical permeability coefficient, Π_v, as the key internal parameter. Other internal parameters, such as snow density in the radiative transfer scheme (ρ_{snow}) and bottom melt rate (w_{bot}), were found to have less effect on the pond evolution. For each of the initial variables and internal parameters that do not significantly affect the results, we choose a single, default value listed in Table 1. These values are generally based on ice profiles taken during 2009, for example, the ice salinity and temperature at the beginning of the simulation [see *Polashenski et al.*, 2012]. For the remainder of this paper, we use these default values for all simulations.

For the three key variables: vertical permeability coefficient, initial sea ice thickness, and initial minimum snow depth, we performed a number of simulations applying values over the ranges given in Tables 2 and 3, using an iterative process. We compared the resulting time series of pond fraction to the observed values presented in Figure 2 to

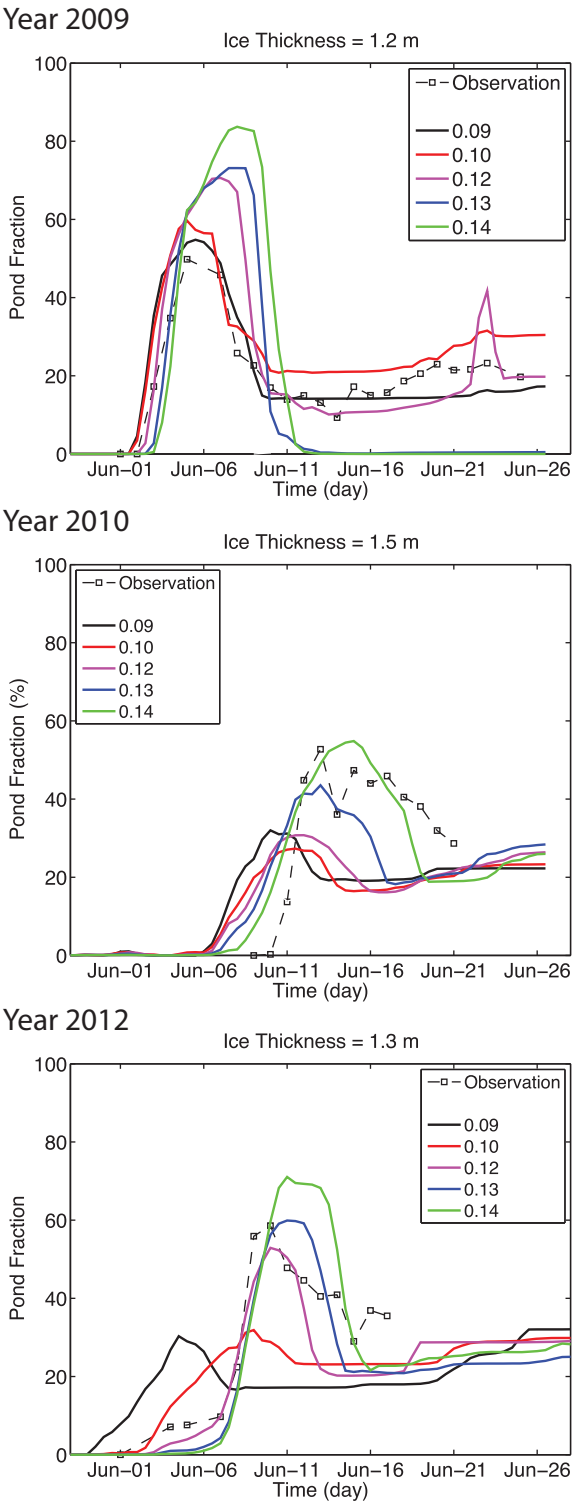

Figure 6. Pond fraction (%) for a range of initial minimum snow depths (m), using the optimal internal parameters and the optimal initial ice thickness for (a) 2009, (b) 2010, and (c) 2012. Dashed lines are observed pond fraction.

determine the optimal Π_v, and, for each of the 3 years, the optimal initial ice thickness and minimum snow depth. Overall, our goal was for the model to generate a pond evolution similar to the observations, with initial flooding followed by pond drainage and then a more stable pond fraction dependent on the amount of sea ice lying below sea level. A successful simulation is one where pond formation (stage 1) begins on approximately the correct date; the maximum flooding, at the transition from stage 1 to stage 2, covers a fractional area similar to observations; and drainage leads to a correct pond fraction when the pond surfaces are at sea level (beginning of stage 3). Unfortunately, we do not have data beyond the stage 2/stage 3 boundary (minimum pond extent following drainage) for 2010 and 2012.

In the following sections, we examine the sensitivity of the model to each of these three variables. For simplicity, we first show time series ensembles where only one parameter is varied with other parameters held fixed at the optimal values given in Tables 2 and 3 (e.g., Figures 5 and 6). We also present two-dimensional ensembles of maximum and minimum pond fraction where the two initial condition parameters, minimum snow depth and ice thickness, are varied (e.g., Figure 8). This allows easier identification of the processes that control pond evolution.

4.1. Calibration of Permeability Coefficient

We first focus on the permeability coefficient, Π_v, which sets the rate for water percolation through brine channels in the ice. Table 2 lists the range of values that are considered for this variable, and the default values are used for all other variables. Figure 5 shows the melt pond fractions (as the percent of grid points that are ponds, where $h_p > h_{is} + 0.02$ m as described in section 2) for this range of Π_v for each year. In general, the model is more sensitive to this parameter for 2009 in comparison with 2010 and 2012. For 2009, the smallest Π_v generates a permanently flooded scenario, and the largest values lead to complete drainage and no ponds after the initial flooding event. Sensitivity to Π_v in 2010 and 2012 is less severe; however, in all cases, applying a value of $\Pi_v = 1 \times 10^{-9}$ leads to a nearly pond free surface after drainage. Overall, the starting date of ponds is within a day or two of the observations and the value of the permeability coefficient has little effect on this date.

Table 4. Optimal Values of Initial Minimum Snow Depth and Ice Thickness Along With Maximum Flood Pond Fraction and Pond Fraction at the Last Observation Time[a]

Year	h_{init} (m)	h_{snow} (m)	Flood Fraction (%)	End Fraction (%)
2009	1.2	0.09	55 (50)	18 (20)
2010	1.5	0.14	55 (55)	20 (29)
2012	1.3	0.13	61 (59)	20 (36)

[a]Observed values are in parenthesis.

Our analysis indicates that the value of $\Pi_v = 1 \times 10^{-10}$ m^2 yields a reasonable fit between the simulated and observed pond fraction behavior as measured by the timing and value of the peak pond fraction and resulting pond fraction at the end of the measured record. Values too small lead to excessive flooding that does not sufficiently drain the ice surface, leaving pond coverage that is often too high. Larger values tend to drain pond water before ponds can preferentially melt sea ice, leaving an insufficient number of ponds below sea level after drainage is complete. That is, stage 2 starts too early, so the pond fraction at the beginning of stage 3 is too small. For both 2010 and 2012, the optimal permeability coefficient yields a pond fraction at the end of the observed record that is less than the measured value by about 10–15%. We note that our model is limited to level ice and does not account for variations in the ice topography or leads that would prevent unrealistic flooding. Consequently, smaller values for Π_v might be more appropriate if the model is initialized with spatially varying ice thickness.

4.2. Sensitivity to Initial Minimum Snow Depth

We next examine the sensitivity of the pond fraction to initial minimum snow depth (Figure 6). Unlike Π_v, we determine the best-fit minimum snow depth for each year separately. As before, default values for the other variables (Table 1) are used along with the optimal permeability (section 4.1), and initial ice thicknesses for each year (section 4.3). A summary of all optimal parameters is presented in Table 4.

Overall snow cover contributes to the fresh water budget that is key in the formation of ponds. For example, if the snow cover is very thin, then fresh water is limited to just the drained upper ice contained in the ice freeboard. Increasing the initial minimum snow depth is equivalent to adding potentially more melt water that can fill ponds. Consequently, in most of the simulations, maximum flooding corresponds to deeper initial snow cover. Initial minimum snow depth can also have a significant effect on the initial pond formation date, with shallow initial snow in some cases accelerating the formation of ponds (especially for 2010 and 2012). Snow depth also affects the pond coverage after drainage in year 2009. This suggests that initial snow cover thickness in year 2009 was not the primary factor in the initiation of melt pond formation but had a greater control on the pond coverage after flooding.

We note that the minimum snow depth does not necessarily agree with field observations of snow depth during each of the test years. Snow surveys often show regions of minimum snow depth that are less than the values that were optimal for our simulations. Other factors, such as variations in the ice thickness, also could be affecting the formation of ponds. An example is given in *Landy et al.* [2014], where initial snow topography did not always correspond to actual snow thickness, but was in some locations indicative of an ice hummock where ice was noticeably thicker than the surrounding region. Here we view the minimum snow depth as a descriptor that takes into account the overall snow and ice thickness variations, rather than an absolute value for the minimum snow depth.

4.3. Sensitivity to Initial Sea Ice Thickness

The initial ice thickness (Figure 7) is important in determining the evolution of modeled ponds, but to a lesser degree than the initial minimum snow depth. Measurements of ice thickness are only available at single points during the three study years and are not reliable given the variation in sea ice thickness generated by differences in snow cover and bottom freezing. Consequently, we explore a range of ice thickness for each year to determine the model sensitivity to this parameter.

Simulation results do not in general show a systematic relationship between pond fraction and the initial ice thickness for the three study years. For 2010 and 2012, the maximum pond fraction (flooding) is generally higher for thinner ice, but the pond fraction tends to converge after drainage to a consistent value

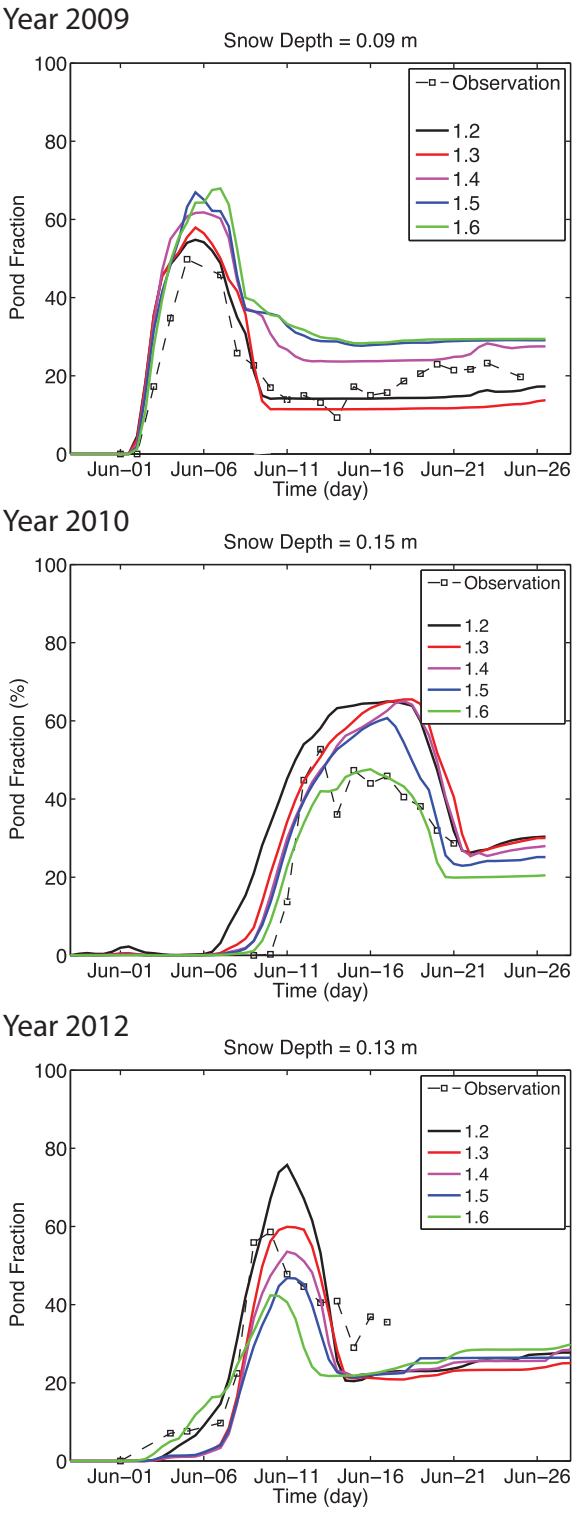

Figure 7. Same as Figure 8, but for a range of initial ice thickness (m), using the best-fit initial minimum snow depths (m) for (a) 2009, (b) 2010, and (c) 2012.

across all thicknesses. In contrast, year 2009 produces a larger maximum pond fraction for thicker ice, with thinner ice having a noticeably lower pond fraction after drainage. In some cases (2012), thinner ice generates more flooding but the resulting pond fraction after drainage does not show significant differences between the ensemble members.

Ensemble plots of the minimum (following drainage) and maximum pond fraction (Figure 8) show the combined effects of initial ice thickness and minimum snow depth on the pond behavior. Each year displays a different overall relationship. For example, in year 2009, maximum pond fraction is larger for deeper snow cover (Figure 8b). Year 2009 also shows a modest relationship between maximum pond coverage and minimum pond coverage; more flooding corresponds to somewhat reduced pond coverage after drainage. A different behavior is noted in year 2010 where minimum and maximum pond fractions vary more in unison, with high maximum pond fraction corresponding to high minimum pond fraction. As shown in Figures 6 and 7, ponds in 2010 do not drain rapidly after reaching a maximum, with pond fraction remaining constant or decreasing slightly with time. Year 2012 presents a case with less organized behavior. The maximum pond fraction is produced with deeper snow cover and thinner ice, with decreased maximum pond fraction for shallow snow cover and thicker ice. The minimum pond fraction does not have a simple relationship with either sea ice thickness or minimum snow depth.

The formation of sea level ponds after drainage depends on how much ponds scour out the sea ice beneath the ponds during the initial flood stage. Scouring beneath ponds is produced by increased melting relative to adjacent snow covered ice that has much higher reflectance of solar radiation. We would expect that thinner initial sea ice would lead to more sea level ponds after drainage because less scouring is necessary to form a below-sea-level depression. This effect seems to be active in 2010 (Figures 7 and 8) where the minimum pond fraction generally increases slightly as sea ice thickness decreases. In the other cases, the minimum pond fraction does not show a significant relationship with the ice thickness with only small difference in pond fraction toward the end of the simulations.

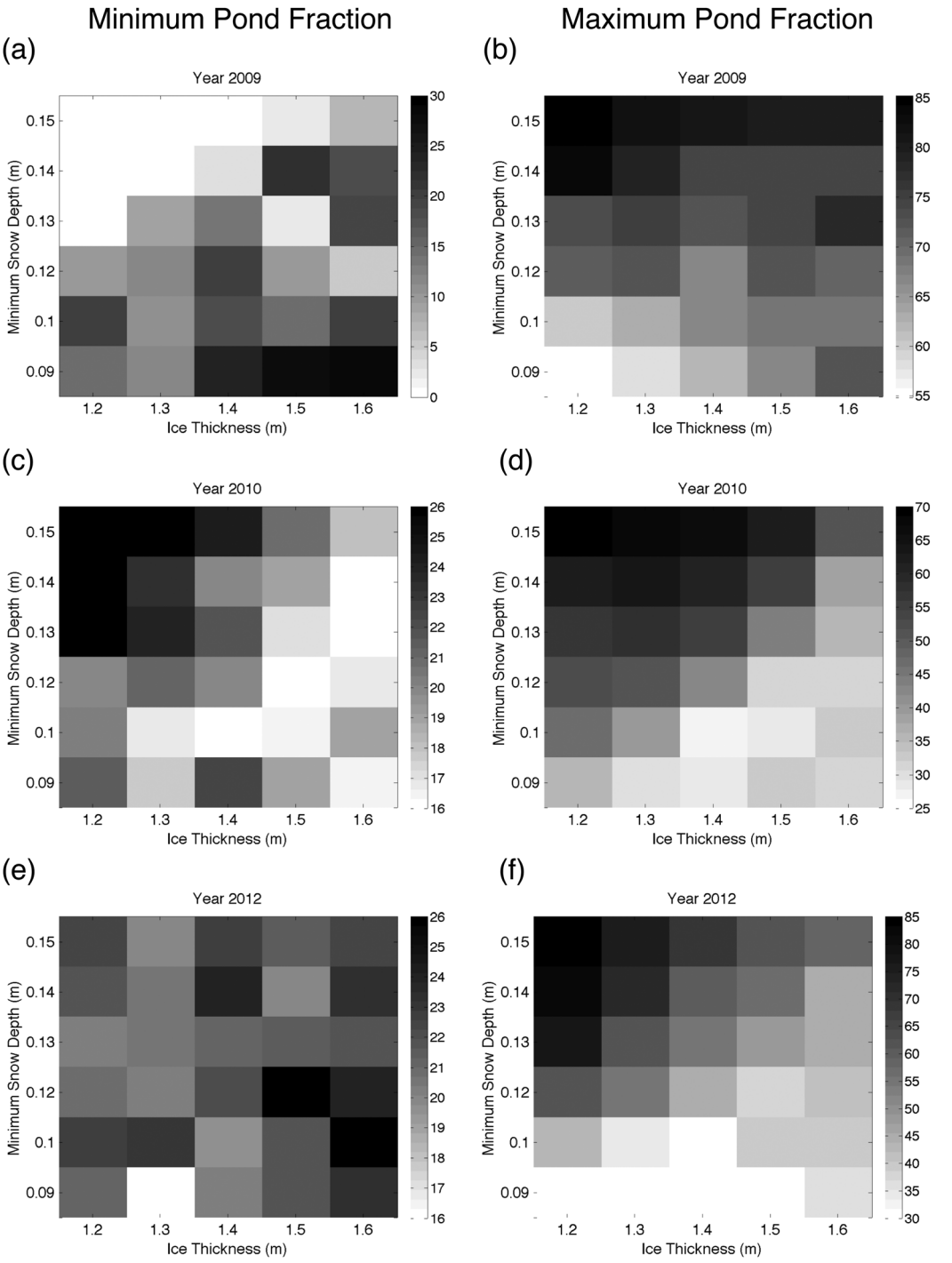

Figure 8. Minimum (postdrainage) and maximum pond fraction as a function of initial minimum snow depth and ice thickness for (a and b) 2009, (c and d) 2010, and (e and f) 2012.

5. Basic Case Pond Fraction and Albedo

Calibration of the model was performed using the average pond coverage over time as summarized for each year in Figure 9. Overall, the differences between the observed and simulation pond fractions are typically within 10%, which is reasonable given the uncertainty in measured snow depth and ice thickness. Nevertheless, it is clear that the model has an unrealistically large sensitivity to some of the parameters. For example, assuming a thicker snow cover in 2009 greatly decreases the pond coverage following drainage

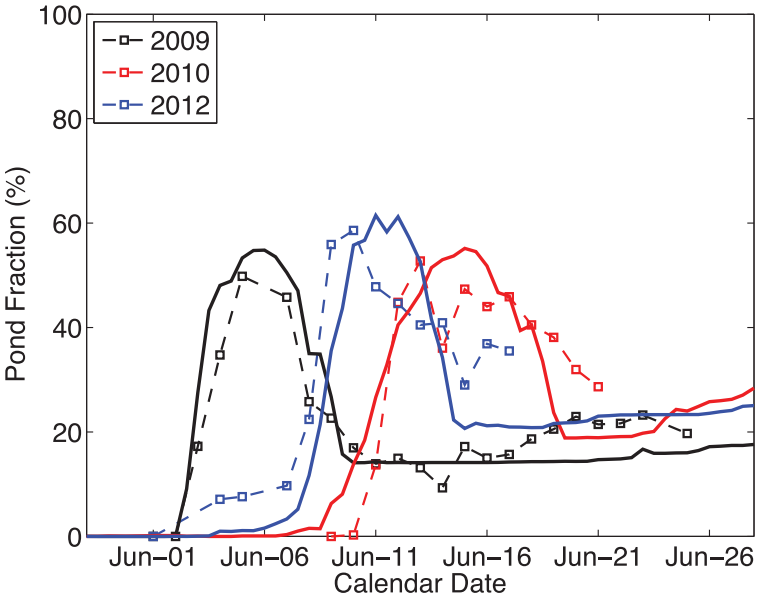

Figure 9. Observed (dashed) and simulated (solid) pond fraction using optimal internal parameters (Table 3) and initial conditions for each year (Table 4).

as shown in Figure 6, whereas observations suggest that postdrainage pond coverage does not often collapse to near zero values.

Through the remainder of this paper, we examine the "base case" simulations shown in Figure 9, which use the default values for all initial conditions and internal model parameters for a given year (Tables (1–4)). Our goal is to compare these best-case simulations with observed properties from the field and evaluate how well the model is able to duplicate pond features, such as overall albedo, pond shape, and connectivity. We also examine the simulated ice vertical structure to better understand the processes that lead to flooding and pond drainage.

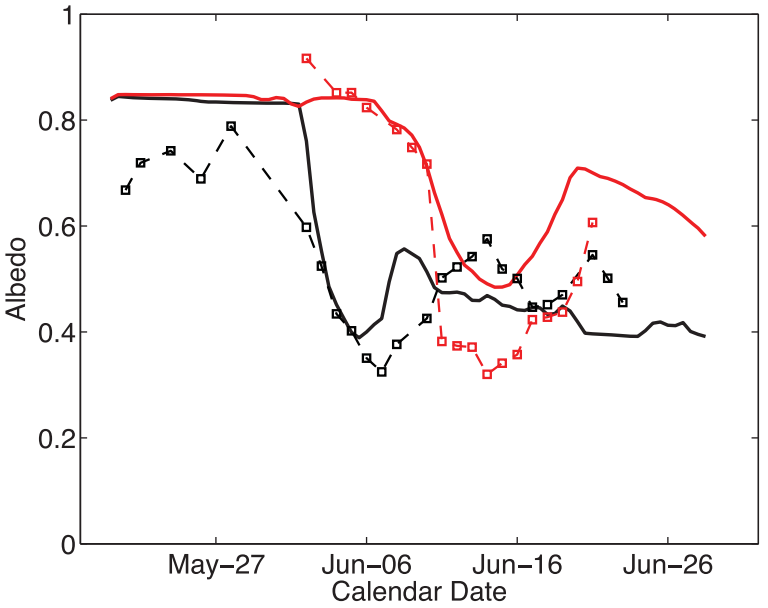

Figure 10. Model predicted (solid) and observed (dashed) surface albedo for 2009 (black) and 2010 (red).

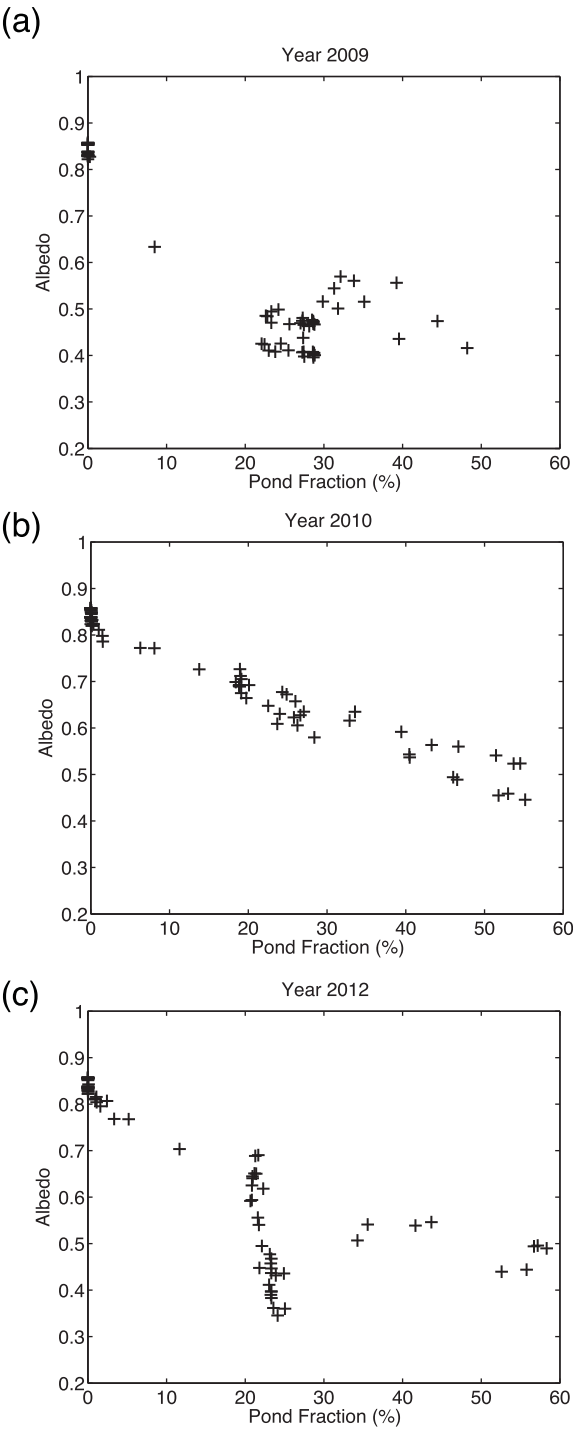

Figure 11. Modeled albedo as function of pond fraction for basic case simulations for (a) 2009, (b) 2010, and (c) 2012. Points are taken every 12 h over 40 days.

5.1. Basic Case Albedo

Average surface albedo is an important metric that can help in understanding differences between the model and measurements. Surface albedo measurements were taken along the survey line adjacent to the LiDAR observations in 2009 and 2010. From the model we can estimate albedo using

$$A_t = 1 - \frac{R_{abs}}{(R_{sw} + \varepsilon)}, \tag{6}$$

where R_{abs} is the shortwave and near infrared radiation absorbed by the ice and ocean, R_{sw} is the incident downwelling shortwave and near infrared radiation, and $\varepsilon = 0.001$ is a small constant to prevent numerical overflow. We calculate A_t by averaging the albedo from each of the grid cells. Plots of the observed and model average albedo are shown in Figure 10. Simulated albedo for both model years follows the general trend of decreasing albedo over time. Initially, the albedo is relatively constant at about 0.8, representing typical snow cover before significant melting. The observed albedo drops rapidly with the onset of ponding, reaching average values in both years that are less than 0.4 along the survey line. In the simulations, flooding generates a significant drop in albedo for both years (∼0.4 in 2009 and ∼0.3 in 2010), but the decreases are not quite as large as the observed values (∼0.5 decrease in both sets of observations). Simulated albedo increases during drainage as in the measurements, followed by a downward trend as the ice thins toward the end of the record.

Average albedo is affected by both the areal coverage and the depth of melt ponds, as deeper ponds have lower albedo. We can diagnose these two effects in the simulations by plotting the albedo as a function of pond fraction for the base case simulations (Figure 11). Generally, albedo decreases linearly as a function of pond fraction, with each year displaying roughly the same relationship (excluding the complex behavior between 20 and 30% pond fraction). For example, a typical albedo value for a pond fraction of 40% is about 0.6. The effects of deepening ponds on albedo are noticeable when the spread of albedo values is large for a given near-constant pond fraction. For 2009 and 2012, we note a larger spread of albedo values when the ponds are at roughly 20–30% coverage, representing the time period of sea-level ponds. Albedo at these times decreases mostly because of pond deepening, with pond fraction only increasing a small amount (this is shown more clearly in 2012).

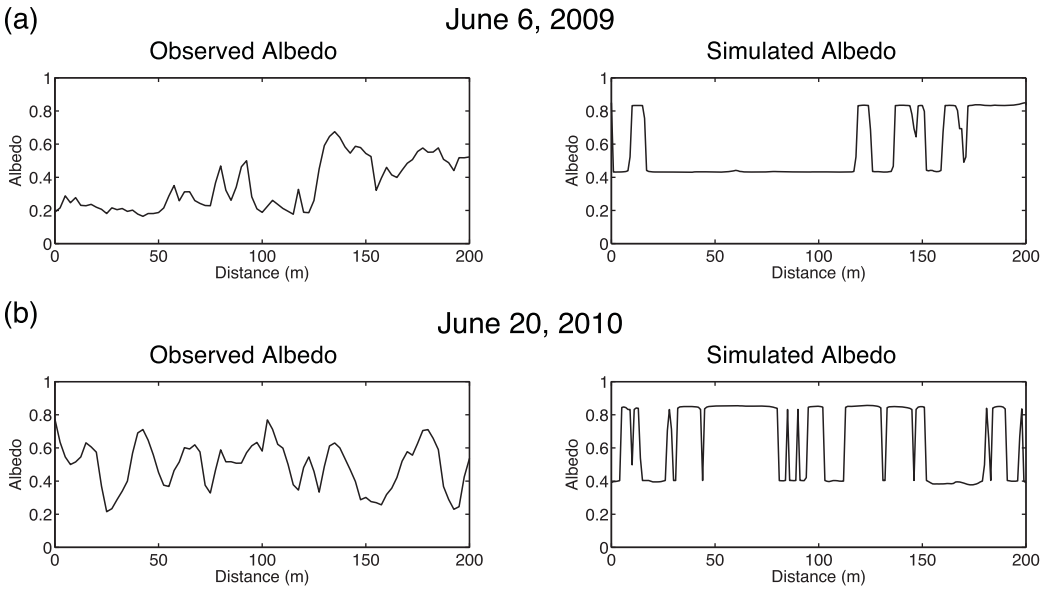

Figure 12. (left) Observed albedo along the survey line and (right) modeled albedo from $x = 10$ m for (a) 6 June 2009 and (b) 20 June 2010. Observations are a running average over a distance of 2.5 m; simulated values are from each grid point with 1 m separation.

Comparisons of measured versus simulated albedo cross sections provide another diagnostic for assessing the importance of pond coverage and depth (Figure 12). On broad scales, the albedo characteristics in the measured fields and model results are in rough agreement. For example, the 2009 case has generally lower albedo associated with ponds between 0 and 125 m in both plots; 2010 has a more uniform variability across the domain, with ponds appearing as local minima in albedo. Absolute values of the albedo, however, are quite different in the observations and model, with the measured pond albedos consistently lower than the simulated pond values. Measured pond albedo is often near 0.2 in 2009 and frequently displays local minima in 2010 that are near 0.2. In contrast, the simulated pond albedo never falls below 0.4 in either year, and tends to have just two discrete values rather than the more uniform variability noted in the measurements.

Observed albedo was estimated by performing a running average of albedo measurements over a 2.5 m distance, which partially explains why the observations have a smooth spatial character. Other differences between the simulated and observed albedo variations are likely due to use of a single snow grain size, which effectively sets the ice and snow surface albedo, and the use of a threshold liquid water height, $h_{is} - h_p = 0.0$ m, for determining if the surface is treated as pond covered in the radiative transfer scheme or as a snow/ice surface. We note that this transition is only applicable to the radiative transfer model in determining the surface type (as described in section 2), and is distinct from the pond threshold used to determine when ponds are thermodynamically active in the model (i.e., when h_p exceeds h_{is} by 0.02 m, see supporting information). During the actual melting process, melt water gradually changes the albedo as voids between snow and ice fill with water. This effect is not currently included in the model. Aerial photographs, presented in the next section, qualitatively show how flooding leads to a smooth transition from snow-covered to pond-covered ice. Sediments in the observed sea ice and ponds are also evident in the photographs and currently are not included in the model, which could partially explain the simulated higher overall albedo values.

5.2. Basic Cases: Evolution of Spatial Characteristics

Changes in simulated pond fraction can be related to observed pond coverage by comparing the pond depth at various times in the simulation with aerial photographs from year 2009 (Figure 13). Comparisons are shown for pond evolution stages 1 and 3 [*Eicken et al.*, 2002]. Flooding in the model during stage 1 is well represented as shown by comparing pond depth with the aerial coverage in Figure 13a. In general, modeled ponds correspond to areas of lower ice and snow thickness. Pond-free ice area is consistent between the two images; however, gray regions in the aerial image show that sediment and wet snow can affect the albedo. Deeper snow in the upper

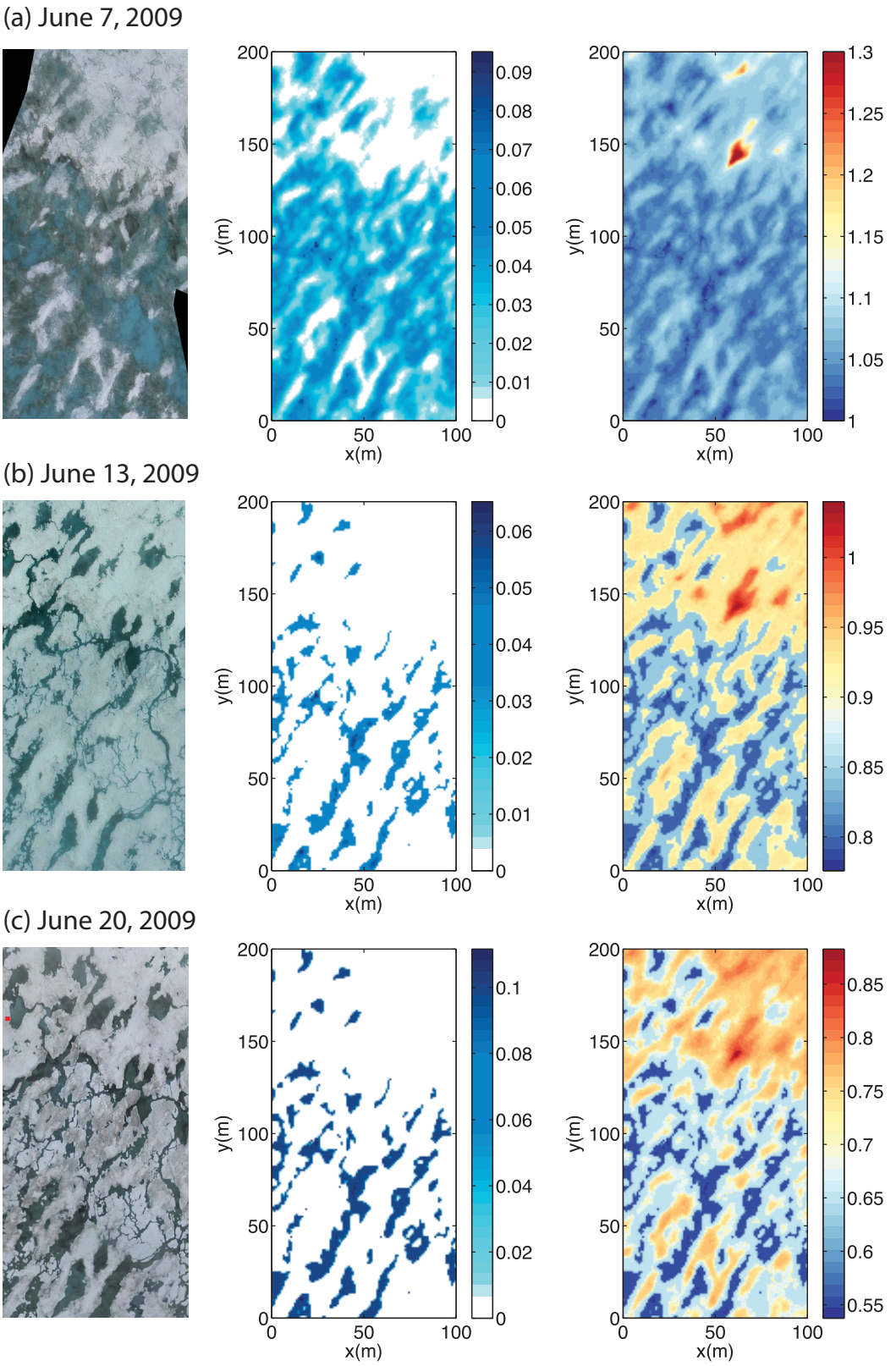

Figure 13. Aerial photograph of ice surface (left), model simulated pond depth (m, middle), and ice + snow thickness (m, right) for (a) 7th June (Stage 1), (b) 13th (early Stage 3), and (c) 20th (late Stage 3) of 2009. Note the different color bar scales for each date.

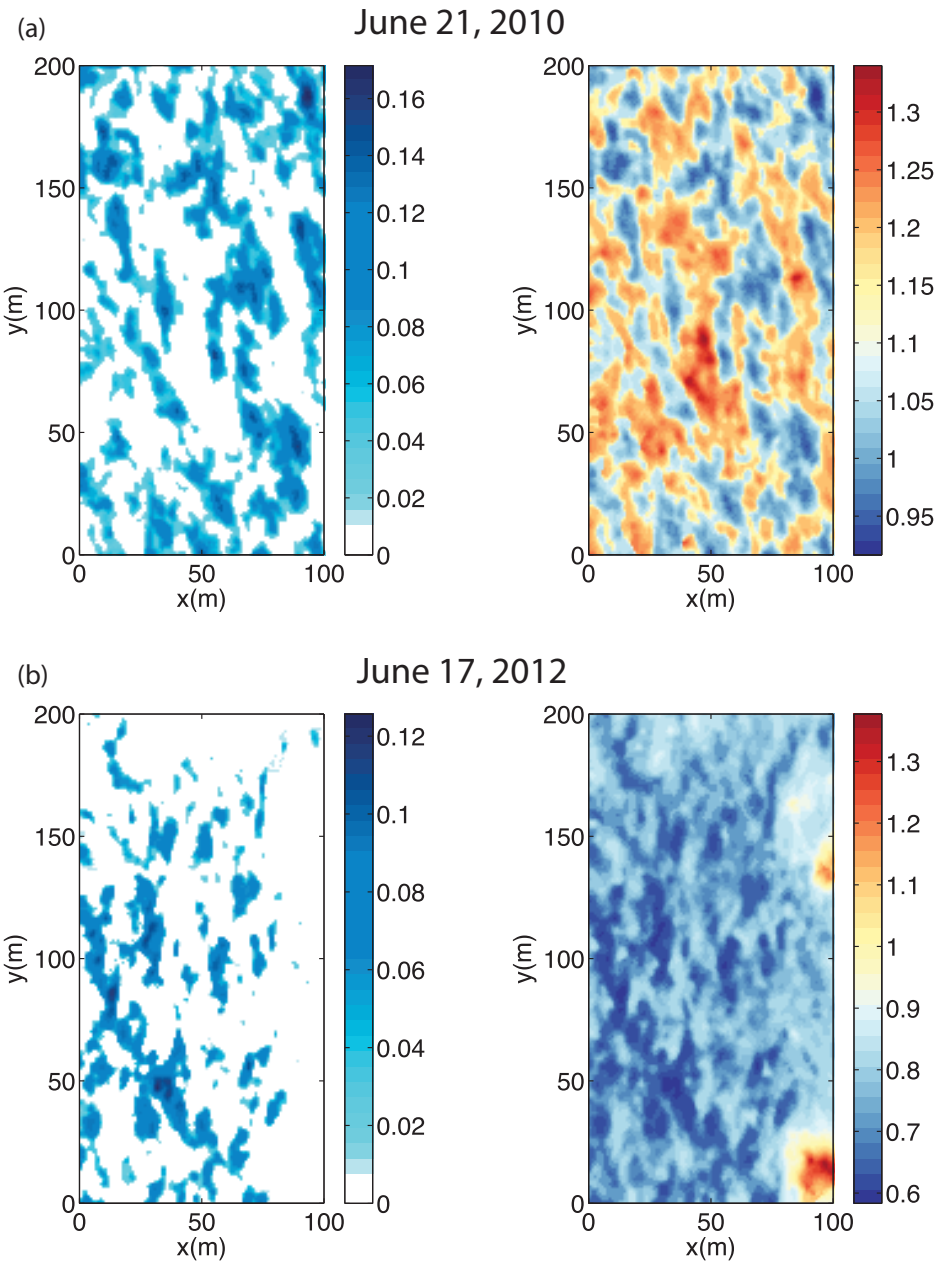

Figure 14. Simulated pond depth (m, left) and ice and snow thickness (m, right) for (a) 21 June 2010 and (b) 17 June 2012. Plots represent ponds during late stage 2 when ponds are near sea level height.

third of the domain limits flooding, so that ponds are mostly confined to the lower two thirds of the region. After draining (i.e., at the beginning of stage 3), inconsistencies between the model and aerial image are apparent for the location, size, and shape of ponds (Figure 13b). In particular, the observed ponds tend to form channels connecting larger ponds, whereas the model does not represent this behavior. In the model, horizontal melt water transport is instantaneous, which cannot preferentially melt ice like water moving through channels on the ice surface. Overall, however, modeled ponds tend to follow the pattern shown in the aerial image even though individual features are not as well represented. Ponds in the last image, which is late in stage 3, tend to show the best agreement in size and location for areas without drainage channels, for example, in the bottom quarter of the domain. Smaller ponds are generated in drainage channels, for example between the large ponds in the photograph, suggesting that movement of water on the top of the ice has a significant impact on the location of long-lived ponds and probably contributes to a larger pond fraction at later times.

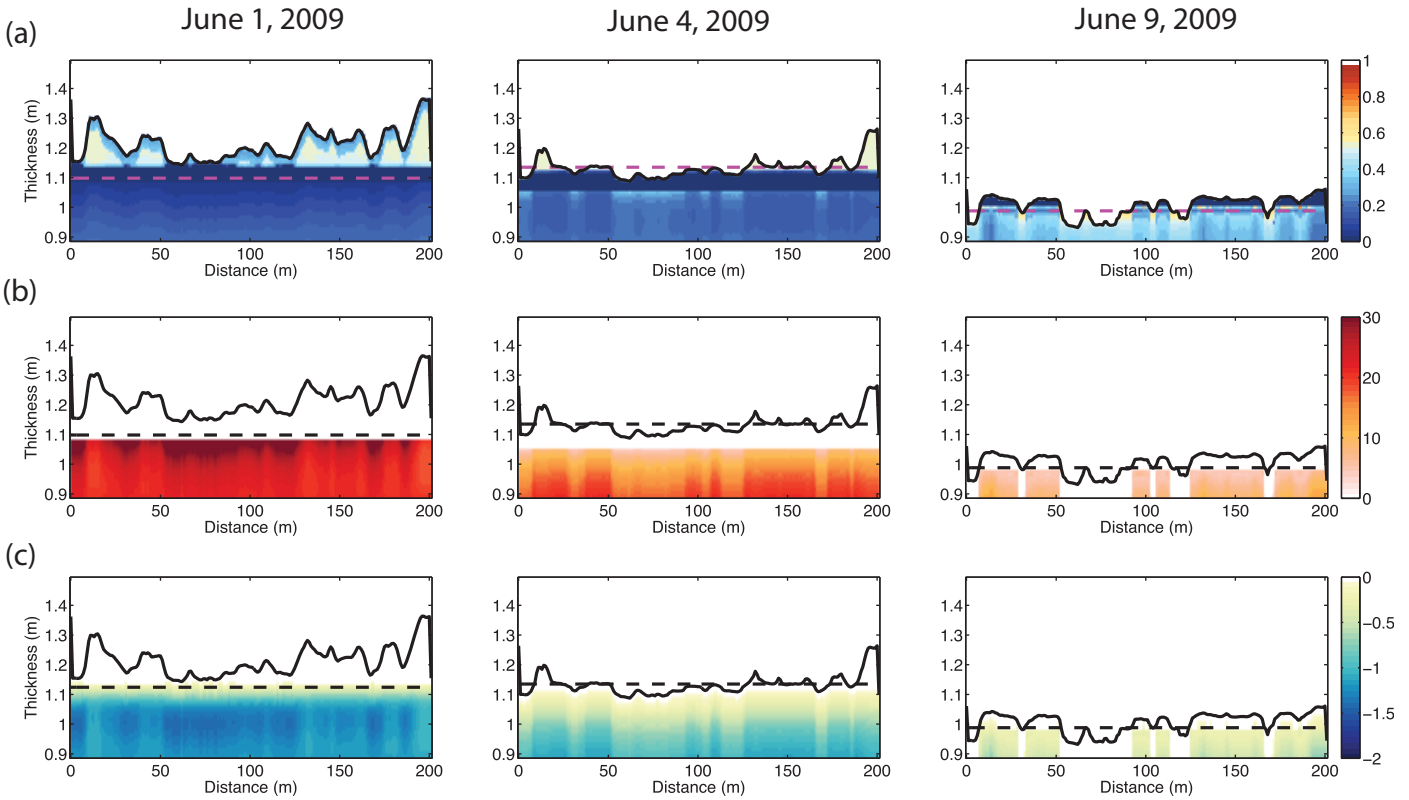

Figure 15. Vertical cross sections along $x = 50$ m at three different times for (a) void fraction ($1 - \phi$), (b) salinity (psu), and (c) temperature (°C) for 2009. Also shown are the location of the snow/ice surface (solid) and the water table (dashed). Ponds are located where the water table is higher than the snow/ice level.

Plots of the pond coverage and ice/snow thickness for the 2010 and 2012 case demonstrate pond behavior for late stage 2 (Figure 14). Ponds flood low-lying areas in the snowfield as shown by the collocation of ponds and minimum ice and snow thickness. After drainage, ponds occupy regions where the ice has preferentially melted from the lower pond albedo. Comparison between the simulated ponded regions and ponds inferred from the LiDAR data shows similar features (not shown).

5.3. Frozen Layer Time Evolution

The basic processes that lead to the formation of surface melt ponds are controlled largely by the interaction between relatively cold, brine-filled ice and fresh water released by snow and ice melt at the surface. Key in this process is the conductive heat flux between grid cells that are salty and relatively cold with overlying grid cells that contain fresher water and are relatively warm. For both grid cells, the local temperature is fixed at the freezing point, which is set by the brine salinity. Because the fresh water cells are warmer than the underlying brine-filled cells, heat is lost from the fresh water cells to the brine-filled cells. As the brine solution in the salty grid cell warms, a portion of the conductive heat flux causes melting of the ice. At the same time, heat loss in the fresh water cell causes ice to form, until the cell is eventually completely ice-filled. This process leads to the generation of ice layers that trap surface melt water. A similar process is commonly used in ice cream makers with an ice/salt solution providing the subfreezing temperatures.

Ice layers typically form where the fresh water in snow or empty brine channels overlies brine-filled ice at sea level. Ice temperatures follow the freezing temperature appropriate for the local brine salinity. The resulting vertical structure in the model is shown by plotting void fraction, salinity, and temperature vertical-horizontal cross sections at three different times from the simulation of year 2009 (Figure 15). At the first time (1 June), the ice has already formed a layer of solid ice (void fraction = 0.0) between the water table height, indicated by the dashed line, and the ice/snow surface. Nearly all of the water melted by solar heating of the snow has refrozen in this layer, which is why the water table is below the frozen layer. Snow in this plot is indicated by the significantly higher void fraction above ~1.15 m.

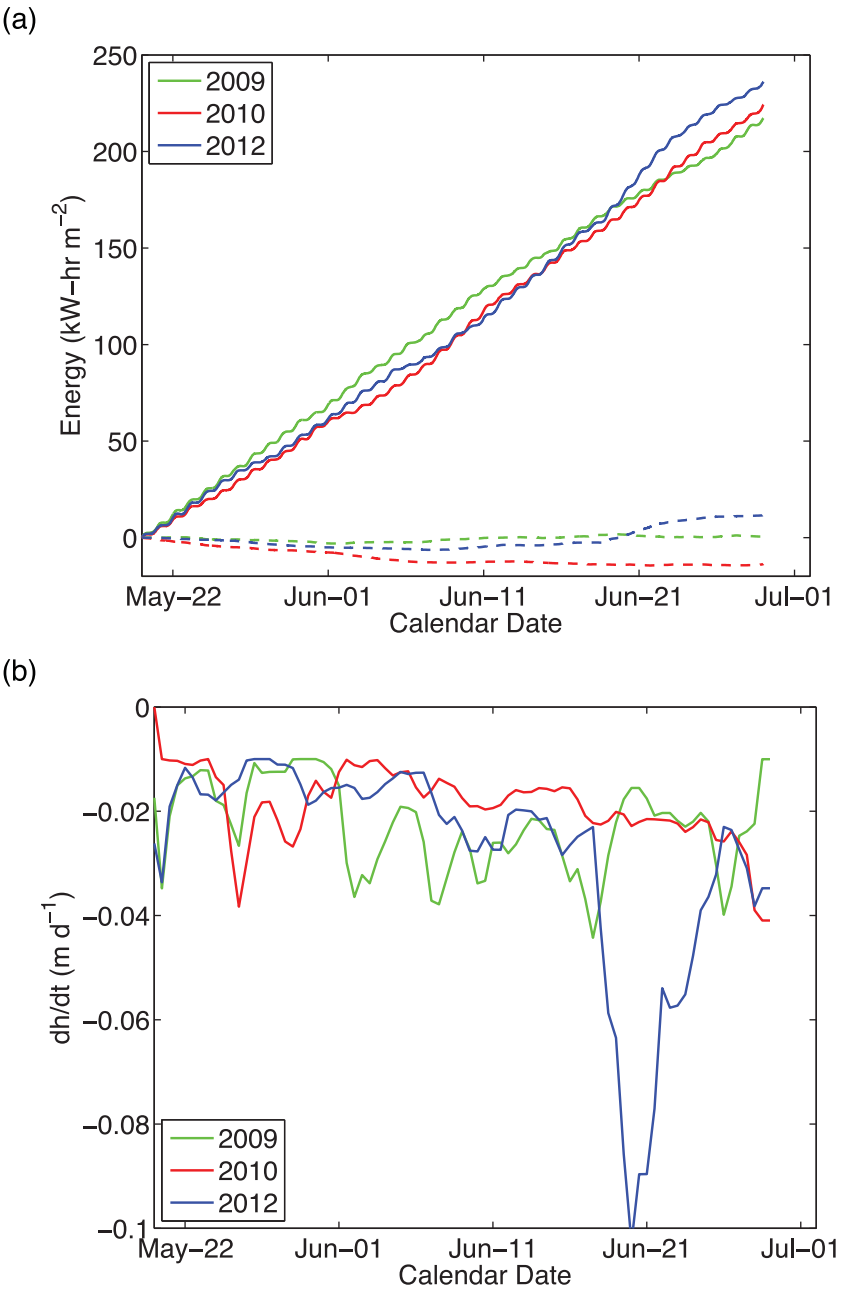

Figure 16. (a) Time-integrated cumulative sum of net longwave, sensible, and latent heat flux (dashed) and with total short wave solar flux (solid) and (b) ablation rate of the horizontally averaged snow and ice thickness. The short-wave flux is the incident radiation and does not account for the surface albedo. All fluxes are averaged over the surface.

As more snow melts (4 June), the water table increases to a level above the surface, resulting in flooding as shown by regions where the dashed line is above the solid line. By this time, water has started melting through the ice layer, flushing some of the salinity from the ice. Eventually, the frozen layer beneath the ponded regions thaws completely, and the salinity of the ice reduces to near zero. Stronger melting of ice under ponds compared with snow covered and bare ice generates large depressions that remain filled with water when the ice drains to sea level.

The formation of impermeable ice layers or superimposed ice in the model is similar to observations reported in *Eicken et al*. [2004] showing the importance of superimposed ice on pond formation and longevity. Here impermeable layers form both in brine channels and, after the channels are plugged, on top of

the ice as melt water drains vertically. The specific location of melt water refreezing in the model is set by the sea level height because that is where the ice temperature is maintained below freezing by the brine. In reality, brine channels higher in the ice column could freeze completely closed before allowing fresh water to penetrate to sea level. More measurements of melt water penetration in the field are needed to clarify this process.

6. Discussion and Conclusions

Development of realistic sea ice models with accurate melt pond representation has been hampered by the lack of detailed measurements of ice thickness and snow properties. The importance of these parameters has only recently been identified through field observations showing that pond formation is highly dependent on the surface topography of snow-covered ice at the beginning of the melt season [*Polashenski et al*., 2012; *Landy et al*., 2014]. In this paper, we develop a sea ice model that uses snow cover topography to predict the evolution of melt ponds for typical first-year sea ice. The model is similar to the ice model presented in *Scott and Feltham* [2010] and *Notz and Worster* [2006], with ice, snow, and pond water simulated using a three-dimensional Cartesian grid. The model is coupled with a radiative transfer model and parameterized movement of brine via a Darcy velocity based hydrological approach. Three different melt seasons are used to calibrate the model for the prediction of melt pond fraction as a function of time. Overall, our results demonstrate the importance of snow cover in determining melt pond coverage as suggested by *Polashenski et al*. [2012].

A significant finding of this work concerns the sensitivity of melt pond area fraction to the permeability of the ice. Observations suggest that the volume fraction varies significantly as melt water refreezes in ice pores during early melt [*Polashenski et al*., 2012; *Landy et al*., 2014]. Frozen layers can effectively prevent melt water from draining through the ice until the ice warms sufficiently for flaws to develop. As flaws grow, surface melt water occasionally drains rapidly so that the entire system changes abruptly, or in other cases drains slowly over a period of days to weeks. We determined that using a permeability coefficient based on brine-filled ice [e.g., *Golden et al*., 2007] generates too much drainage of melt water, limiting pond fractions after drainage. In our model, a permeability coefficient roughly 100 times smaller was needed in most cases to prevent excessive drainage and reduced pond fractions. The low values of vertical permeability required to explain meltwater pooling are in line with observations of the importance of a comparatively thin surface ice layer in retaining meltwater at the surface [*Eicken et al*., 2004].

Results from our experiments also suggest that the time when ponds first form is a function of both the specific snow surface topography and the total heat received by the ice surface. For the three years examined here, the order of pond formation dates was earliest for 2009 and latest for 2010 (see Figure 2). Plots of the integrated energy flux at the ice surface (Figure 16) agree with this pattern before 10 June, showing the highest cumulative heating (note that this is the total downwelling shortwave radiation and does not account for albedo change) for 2009, with less heating for 2010 and 2012. Also shown in Figure 16 is the average ablation rate for each of the study years. Outside of the large peak on 20 June 2012, year-to-year variations in melting rate are relatively consistent with values around -0.02 m d^{-1} (this includes a constant -0.01 m d^{-1} imposed bottom melting rate). These values are comparable with measured ablation rates in the central Arctic Ocean, for example, as presented in *Eicken et al*. [2002], but are smaller than the maximum rate of -0.05 m d^{-1} measured at the Barrow site for 2001 [*Grenfell et al*., 2006]. Overall, the ablation rate does not show a significant pattern that can be directly related to differences between the pond fraction coverage in the three cases.

To test the importance of snow topography versus forcing, we ran the model using the 2010 and 2012 snow topographies, but with the surface heat flux forcing from 2009. Results from these experiments (not shown) generated ponding at about the same time as those with the original forcing. Consequently, it would appear that the weather conditions during the melt season, while important, do not totally control the formation time of ponds.

The timing of pond drainage after the initial flooding is critical for determining the extent of ponds after the surface has drained to sea level. If drainage is too early, then ponds do not have sufficient time to preferentially melt the ice below them (compared with surrounding ice) to create below-sea-level ice topography, and thus melt pond fraction is unrealistically low postdrainage. Drainage too late causes too much

flooding, and the wide extent of ponds results in similar melting across much of the ice surface. Again, the differential melting is insufficient for postdrainage ponds. Consequently, long-lived ponds in the model are only possible for specific conditions of minimum snow depth and snow properties that fit a optimal duration of flooding. The model is reasonably consistent with measurements in showing that deeper snow cover delays the formation of ponds and leads to more extensive pond coverage during the flooding stage. We also found that, for each year in our study, the minimum snow cover was very consistent between about 0.1 and 0.15 m. This suggests that drifting of snow on ice tends to scour away regions so that nearly all the snow is removed, which in the model yields a small but nearly constant minimum snow depth for optimal pond fraction prediction.

Observed pond behavior also appears to be sensitive to snow properties; however, observed ponding rarely has extremes in behavior that are possible using the model. For example, flooding over the ice surface for large regions is typically not observed because melt water will eventually encounter a large flaw or crack in the ice and drain. Observed ponds also have noticeably lower albedos in comparison with the ice model, with values often near 0.2 versus 0.4 in the model. One possible reason for this difference is that the radiative transfer scheme [*Hunke et al*., 2013b] is based on ponding over much thicker ice observed during the SHEBA experiment and may have too much scattering for ice under ponds. Alternatively, we do not parameterize sediment loading in the sea ice model, which has a clear impact on the measured albedo.

Some of the model sensitivity results from the way snow albedo is calculated when the snow is nearly saturated with melt water. The CICE radiative model used here has relatively sharp transitions between pond, snow, and ice surface conditions. These transitions are smoothed for typical CICE large-scale model applications because of multiple ice thickness categories that are used for O(km) scale grid points. In our implementation, the surface type for each grid cell is uniform and determined by the depth of the melt water relative to the height of the snow/ice. When the melt water depth is greater than the surface height, we transition from snow/ice to a pond surface in the radiation scheme, which causes an abrupt lowering of the surface albedo for the grid point. This lower albedo, in turn, increases the rate of surface melting. More field measurements are needed to better define the transition from snow to pond so that this process can be refined over the current approximation.

Understanding the role of snow cover in setting melt pond coverage is important for representing melt ponds in climate models. Both observations and our modeling results suggest that winters with light snow cover will develop less melt pond coverage during flooding because of reduced fresh water during the initial melting stage. Other characteristics of the snow cover, for example the degree of snow dune variability, may also be important in determining the melt pond coverage. Future simulation studies along with more extensive measurements of melt pond systems will help determine if these effects are of first-order importance in determining the spring melt pond fraction.

Acknowledgments

This research was funded by the National Science Foundation grant ARC-1022991. We would like to acknowledge high-performance computing support from Yellowstone (ark:/85065/d7wd3xhc) provided by NCAR's Computational and Information Systems Laboratory, sponsored by the National Science Foundation. Meteorological and net atmospheric radiation data from the U.S. Department of Energy as part of the Atmospheric Radiation Measurement (ARM) Climate Research Facility North Slope Alaska site were used in this study (available at http://www.arm.gov/). We would also like to thank Elizabeth Hunke and one anonymous reviewer for very constructive comments that greatly improved this paper.

References

Barnes, S. (1964), A technique for maximizing details in numerical weather map analysis, *J. Appl. Meteorol.*, *9*(3), 396–409.

Briegleb, B. P., and B. Light (2007), A Delta-Eddington mutiple scattering parameterization for solar radiation in the sea ice component of the community climate system model, *Tech. Note NCAR/TN-472+STR*, Natl. Cent. Atmos. Sci., Boulder, Colo., doi:10.5065/D6B27S71.

Eicken, H., H. R. Krouse, D. Kadko, and D. K. Perovich (2002), Tracer studies of pathways and rates of meltwater transport through Arctic summer sea ice, *J. Geophys. Res.*, *107*(C10), 8046, doi:10.1029/2000/JC000583.

Eicken, H., T. C. Grenfell, D. K. Perovich, J. A. Richter-Menge, and K. Frey (2004), Hydraulic controls of summer Arctic pack ice albedo, *J. Geophys. Res.*, *109*, C08007, doi:10.1029/2003JC001989.

Eicken, H., R. Gradinger, T. Heinrichs, M. Johnson, A. Lovecraft, and M. Kaufman (2012), Automated ice mass balance site (SIZONET), UCAR/NCAR – CISL – ACADIS, Natl. Cent. Atmos. Sci., Boulder, Colo., doi:10.5065/D6MW2F2H.

Feltham, D. L., N. Untersteiner, J. S. Wettlaufer, and M. G. Worster (2006), Sea ice is a mushy layer, *Geophys. Res. Lett.*, *33*, L14501, doi:10.1029/98GL026290.

Flocco, D., D. Schroeder, D. L. Feltham, and E. C. Hunke (2012), Impact of melt ponds on Arctic sea ice simulations, *J. Geophys. Res.*, *117*, C09032, doi:10.1029/2012JC008195.

Golden, K. M., H. Eicken, A. L. Heaton, J. Miner, D. J. Pringle, and J. Zhu (2007), Thermal evolution of permeability and microstructure in sea ice, *Geophys. Res. Lett.*, *34*, L16501, doi:10.1029/2007GL030447.

Grenfell, T. C., D. K. Perovich, H. Eicken, B. Light, J. Harbeck, T. H. George, and A. Mahoney (2006), Energy- and mass-balance observations of the land-ice-ocean-atmosphere system near Barrow, Alaska, USA, November 1999 – July 2002, *Ann. Glaciol.*, *44*, 193–199.

Hunke, E. C., D. A. Hebert, and O. Lecomte (2013a), Level-ice melt ponds in the Los Alamos sea ice model, CICE, *Ocean Modell.*, *71*, 26–42.

Hunke, E. C., W. H. Lipscomb, A. K. Turner, N. Jeffery, S. Elliot, (2013b), CICE: The Los Alamos Sea Ice Model, Documentation and Software User's Manual, version 5.0, *Tech. Rep. LA-CC-06–012*, 115 pp., Los Alamos Natl. Lab., Los Alamos, N. M.

Inoue, J., T. Kikuchi, and D. K. Perovich (2008), Effect of heat transmission through melt ponds and ice on melting during summer in the Arctic Ocean, *J. Geophys. Res.*, *113*, C05020, doi:10.1029/2007JC004182.

Jonas, T., C. Marty, and J. Magnusson (2009), Estimating the snow water equivalent from snow depth measurements in the Swiss Alps, *J. Hydrol.*, *378*, 161–167.

Landy, J., J. Ehn, M. Shields, and D. Barber (2014), Surface and melt pond evolution on landfast first-year sea ice in the Canadian Arctic Archipelago, *J. Geophys. Res. Oceans*, *119*, 3054–3075, doi:10.1002/2013JC009617.

Lüthje, M., D. L. Feltham, P. D. Taylor, and M. G. Worster (2006), Modeling the summertime evolution of sea-ice melt ponds, *J. Geophys. Res.*, *111*, C02001, doi:10.1029/2004JC002818.

Notz, D., and M. G. Worster (2006), A 1-D enthalpy model of sea ice, *Ann. Glaciol.*, *44*, 123–128.

Perovich, D. K., and J. A. Richter-Menge (2009), Loss of sea ice in the Arctic, *Annu. Rev. Mar. Sci.*, *1*, 417–441, doi:10.1146/annurev.marine.010908.163805.

Perovich, D. K., T. C. Grenfell, J. A. Richter-Menge, B. Light, W. B. Tucker, and H. Eicken (2003), Thin and thinner: Ice mass balance measurements during SHEBA, *J. Geophys. Res.*, *108*(C3), 8050, doi:10.1029/2001JC001079.

Persson, P. O. G., C. W. Fairall, E. L. Andreas, P. S. Guest, and D. K. Perovich (2002), Measurements near the atmospheric surface flux group tower at SHEBA: Near-surface conditions and surface energy budget, *J. Geophys. Res.*, *107*(C10), 8045, doi:10.1029/2000JC000705.

Petrich, C. H. Eicken, C. M. Polashenski, M. Strum, J. P. Harbeck, D. K. Perovich, and D. C. Finnegan (2012), Snow dunes: A controlling factor of melt pond distribution on Arctic sea ice, *J. Geophys. Res.*, *117*, C09029, doi:10.1029/2012JC008192.

Polashenski, C., D. Perovich, and Z. Courville (2012), The mechanisms of sea ice melt pond formation and evolution, *J. Geophys. Res.*, *117*, C01001, doi:10.1029/2011JC007231.

Schröder, D., D. L. Feltham, D. Flocco, and M. Tsamodas (2014), September Arctic sea-ice minimum predicted by spring melt-pond fraction, *Nat. Clim. Change*, *4*, 353–357, doi:10.1038/NCLIMATE2203.

Scott, F., and D. L. Feltham (2010), A model of the three-dimensional evolution of Arctic melt ponds on first-year and multiyear sea ice, *J. Geophys. Res.*, *115*, C12064, doi:10.1029/2010JC006156.

Skyllingstad, E. D., and C. A. Paulson (2007), A numerical study of melt ponds, *J. Geophys. Res.*, *112*, C08015, doi:10.1029/2006JC003729.

Skyllingstad, E. D., C. A. Paulson, and D. K. Perovich (2009), Simulation of melt pond evolution on level ice, *J. Geophys. Res.*, *114*, C12019, doi:10.1029/2009JC005363.

Stroeve, J. C., M. M. Holland, W. Meier, T. Scambos, and M. Serreze (2007), Arctic sea ice decline: Faster than forecast, *Geophys. Res. Lett.*, *34*, L09501, doi:10.1029/2007GL029703.